

CALIFORNIA STATE UNIVERSITY, NORTHRIDGE

Role of Network Connectivity and Fluctuations in the Nucleation of Calcium Waves in
Cardiac Cells

A thesis submitted in partial fulfillment of the requirements

For the degree of Master of Science in Physics

By

Gonzalo Hernandez Hernandez

May 2016

The thesis of Gonzalo Hernandez Hernandez is approved:

Dr. Yohannes Shiferaw (Chair)

Date

Dr. Ana Cristrina Cadavid

Date

Dr. Miroslav Peric

Date

California State University, Northridge

Acknowledgements

My deepest gratitude is to my advisor Dr. Yohannes Shiferaw for his support, encouragement and patience in guiding me through this project. It was a journey full of learning and discovery, in which I had the freedom to explore and learn in a stimulating environment.

I would like to thank my thesis committee members Dr. Miroslav Peric and Dr. Ana Christina Cadavid for their support and mentorship. In addition, I would also like to thank all my professors at CSUN for the knowledge they provided in every lecture; which contributed to the achievement of this goal.

In this journey, I have never forgotten the people who inspired me to follow this direction and admiration for science; I'm grateful to my high school teachers; Dan Royster, Stephanie Norton and Jim Broderick for their mentorship and support.

Lastly, I would like to thank my parents Aristeo and Ricarda for their love and support; my brothers Aurelio, Gerardo, Emmanuel and my sister Analida who have inspired and supported me unconditionally. Without the love and support of my family this would have never been possible.

This thesis is based on my first scientific publication with the American Physical Society; "Role of connectivity and fluctuations in the nucleation of calcium waves in cardiac cells", published in the Physical Review E journal.

Table of Contents

| | |
|--|-----|
| Signature Page | ii |
| Acknowledgements | iii |
| List of Figures | vi |
| Abstract | vii |
| | |
| Chapter 1: Introduction. | 1 |
| 1.1 Cardiac mechanics. | 1 |
| 1.2 The excitation-contraction coupling. | 2 |
| 1.3 Cardiac arrhythmias | 4 |
| 1.4 Cardiac arrhythmias initiation. | 5 |
| | |
| Chapter 2: Intracellular calcium release | 8 |
| 2.1 Spontaneous calcium release. | 8 |
| 2.2 Studies of spontaneous calcium waves | 10 |
| 2.3 A new model for the nucleation of calcium waves in cardiac cells | 11 |
| | |
| Chapter 3: A simplified stochastic model of wave nucleation. | 12 |
| 3.1 Physiological connection. | 12 |
| 3.2 The model. | 13 |
| 3.3 System parameters. | 15 |
| 3.4 System spatiotemporal dynamics. | 16 |
| 3.5 Timing and propagation of Ca waves. | 17 |
| 3.6 Steady state dynamics. | 20 |
| | |
| Chapter 4: A deterministic model of wave nucleation initiation. | 24 |
| 4.1 Deterministic mean-field theory. | 24 |

| | |
|---|----|
| 4.2 Steady state dynamics of mean-field theory | 24 |
| 4.3 Role of fluctuations. | 27 |
| 4.4 Linear stability analysis | 30 |
| | |
| Chapter 5: Network structure. | 32 |
| 5.1 Localization of eigenvectors. | 32 |
| 5.2 Stochastic and Deterministic prediction of wave nucleation. | 33 |
| | |
| Chapter 6: Conclusion. | 37 |
| | |
| Bibliography. | 42 |

List of Figures

| | |
|--|----|
| Figure 1.1 The heart electrical conduction system and the normal sinus rhythm..... | 1 |
| Figure 1.2 Ca transport in ventricular myocytes..... | 3 |
| Figure 1.3 ECG of a patient undergoing sudden cardiac arrest..... | 5 |
| Figure 1.4 ECG recording showing the breakdown of the normal sinus rhythm | 6 |
| Figure 1.5 Triggered activity during calcium overload..... | 7 |
| Figure 2.1 RyRs distribution in rat ventricular myocytes..... | 8 |
| Figure 2.2 Experimental snapshot of calcium waves..... | 10 |
| Figure 3.1 Illustration of the Ca signaling architecture..... | 12 |
| Figure 3.2 Model spatiotemporal dynamic..... | 17 |
| Figure 3.3 Model front propagation and phase space..... | 18 |
| Figure 3.4 The average wave nucleation time..... | 19 |
| Figure 3.5 The average activity $\langle \eta(t) \rangle$ vs time for a range of initial conditions..... | 20 |
| Figure 3.6 Plot of $\langle \eta \rangle$ at time $t = 5000ms$ as a function of r | 21 |
| Figure 3.7 The wave propagation threshold and the transition line..... | 22 |
| Figure 4.1 Dynamics of the mean field theory..... | 25 |
| Figure 4.2 The average probability $\langle P(t) \rangle$ vs time for a range of initial conditions..... | 26 |
| Figure 4.3 Phase diagram of the mean field theory..... | 27 |
| Figure 4.4 Properties of the mean field equations with noise..... | 29 |
| Figure 5.1 Ordered components and mapping of leading eigenvector..... | 33 |
| Figure 5.2 Density of nucleation sites and eigenvectors..... | 34 |
| Figure 5.3 Pearson Correlation vs the excitability parameter r | 35 |
| Figure 5.4 Pearson correlation and the leading eigenvector $\vec{\phi}_1$ and the site probability..... | 36 |
| Figure 6.1 Illustration of the system phase diagram..... | 38 |

Abstract

Role of Network Connectivity and Fluctuations in the Nucleation of Calcium Waves in Cardiac Cells

By

Gonzalo Hernandez Hernandez

Master of Science in Physics

Spontaneous calcium release (SCR) occurs when ion channel fluctuations lead to the nucleation of calcium waves in cardiac cells. This phenomenon is important since it has been implicated as a cause of various cardiac arrhythmias. However, to date, it is not understood what determines the timing and location of spontaneous calcium waves within cells. Here, we analyze a simplified model of SCR in which Ca release is modelled as a stochastic processes on a two dimensional network of randomly distributed sites. Using this model we identify the essential parameters describing the system and compute the phase diagram. In particular, we identify a critical line which separates pinned and propagating fronts, and show that above this line wave nucleation is governed by fluctuations and the spatial connectivity of Ca release units. Using a mean field analysis we show that the sites of wave nucleation are predicted by localized eigenvectors of a matrix representing the network connectivity of release sites. This result provides insight on the interplay between connectivity and fluctuations in the genesis of SCR in cardiac myocytes.

Chapter 1: Introduction

1.1 Cardiac mechanics

A normal heartbeat is the result of a single coordinated electrical wave that propagates through the heart producing an orderly contraction of the muscle. This coordinates the heart to pump blood efficiently. Figure 1.1 (a) shows a schematic representation of the heart electrical conduction system. The single coordinated electrical wave originates in the sinoatrial node. Subsequently, the electrical wave advances in the two atria until it reaches the atrioventricular node. The atrioventricular node permits the wave to reach and stimulate the two ventricles or lower chambers of the heart [30]. The electrical activity of the heart can be recorded using an electrocardiogram (ECG). An ECG is a composite recording of all the action potential produced by the nodes and cells of the heart. Fig. 1.1 (b) shows a standard ECG recording of the normal sinus rhythm, each segment in the ECG represents an event of the electrical cycle.

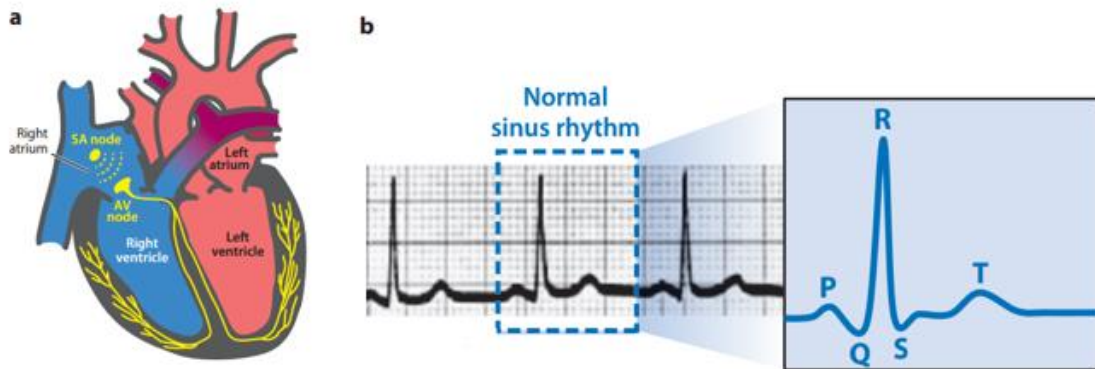


Figure 1.1 The heart and the normal sinus rhythm. (a) Schematic representation of the heart conduction system. (b) Electrocardiogram illustrating the normal sinus rhythm, each segment corresponds to electrical activity of a particular region of the heart; atrial contraction (P-segment), ventricular contraction (QRS-segment) and ventricular depolarization (T-segment) [30].

The sinus rhythm is the product of complex interactions between heart cells (myocytes) forming the heart tissue. The mechanism governing electrical impulses in heart tissue are due to molecular processes at the nanometer scale [30]. The generation of electrical impulses is dictated by the flow of a variety of ions through ion channels implanted in the cell membrane. In myocytes, the ions responsible for electrical activity include; calcium (Ca), sodium (Na^+), and potassium K^+ . These contribute to different phases of the cardiac action potential. The cardiac action potential refers to the transmembrane voltage in response to an electrical stimulus [30]. In other words, as the single coordinated electrical wave advances through the heart, the ions rearrange to create a voltage that responds to an electrical stimulus causing cells to contract.

1.2 The excitation-contraction coupling

Under normal conditions at the cellular level, the mechanical response of the heart relies in the connection between membrane voltage and tissue contraction, commonly known as the excitation-contraction coupling. In the excitation-contraction coupling calcium ion (Ca) is the direct activator of the myofilaments that cause contraction. Furthermore, when Ca is sequestered by the sarcoplasmic reticulum muscle relaxation occurs [2]. In adult mammalian hearts myofilaments related to contraction are structured deep into the complex arrangement of the myocytes. In order to reach into these structures, membrane extensions exist called transverse tubules (t-tubules) [26]. T-tubules spread calcium from the extracellular space to the cell interior.

The process of the excitation-contraction coupling can be summarized in Figure 1.2. As the action potential spreads rapidly across the cell membrane, there is a rapid depolarization phase mainly because of the opening of the sodium (Na) channels. The depolarization

causes the L-type Ca channel to open and introduces a small amount Ca into the cell interior (cytosol). The presence of Ca is sensed by the ryanodine receptors (RyRs) which respond by releasing Ca from the sarcoplasmic reticulum. The collective amount of Ca inside the cell binds to the myofilament protein troponin C which activates the contraction mechanism [2]. **When Ca is used in the contraction process the event of relaxation must follow. To achieve this the cell stores calcium back into the sarcoplasmic reticulum and the rest must be pumped out of the cytosol via two mechanisms; a plasma membrane calcium pump (PMCA) and a sodium/calcium exchanger (NCX) [26]. This is the general transport system of Ca in cardiac myocytes. If myocytes mishandle Ca, in other words if the excitation-contraction coupling fails, this can disturb the sinus rhythm.**

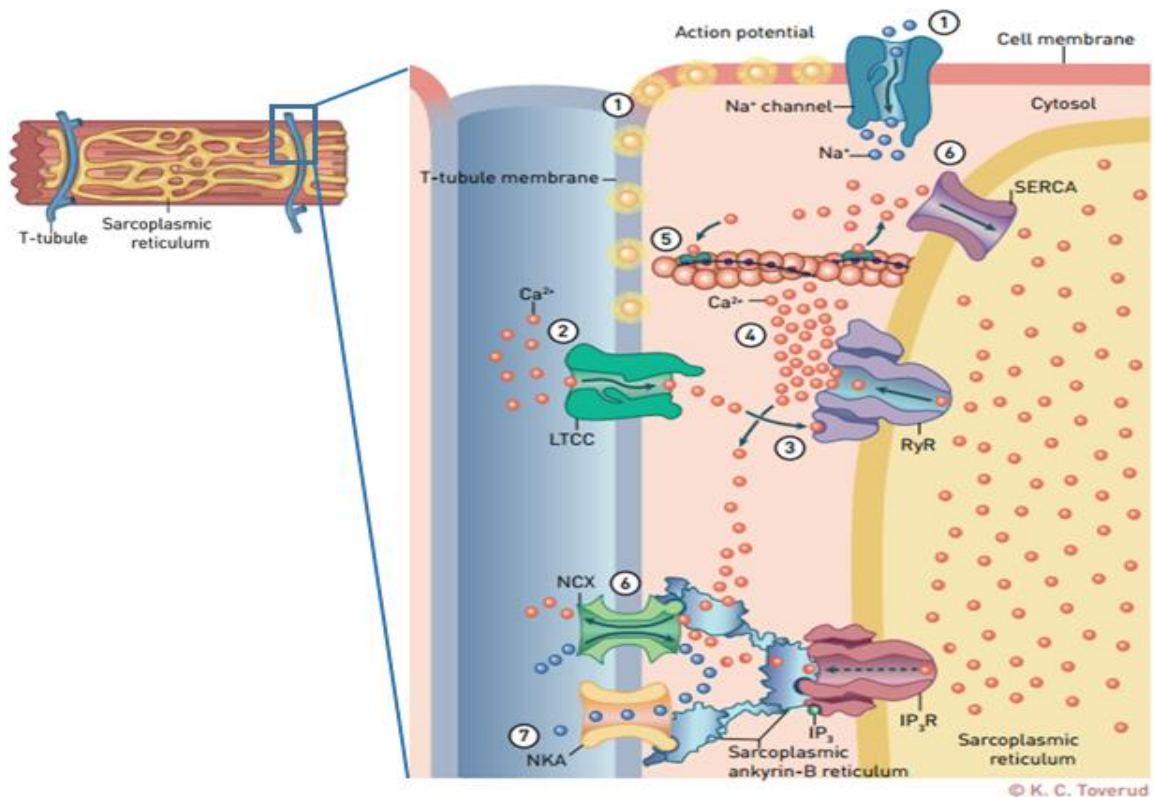


Figure 1.2 Ca transport in ventricular myocytes [31].

1.3 Cardiac arrhythmias

A mechanism that disturbs the sinus normal rhythm of the heart is referred to as an arrhythmia. A normal heart rate is defined as 60 to 100 beats/min, an arrhythmia causing the heart to beat faster than normal rate is called a tachycardia [26]. Tachycardias can occur in different regions of the heart. However, if a tachycardia occurs in the ventricles, it can evolve into a lethal arrhythmia known as ventricular fibrillation (VF) [26]. Ventricular fibrillation causes sudden cardiac death also known as sudden cardiac arrest. Sudden cardiac arrest is responsible for over 300,000 deaths per year in the United States. In addition, it is responsible for half of all heart disease deaths and is the main cause of natural death in the United States [30].

Figure 1.3 (c) illustrates the ECG recording of a patient undergoing sudden cardiac arrest where the sinus rhythm is abruptly disturbed by an event leading to ventricular tachycardia (VT) and consequently evolving into VF. Since the heart is an excitable medium, the event leading to VT in cardiac tissue produces scroll waves that extend in 3D. In two-dimensional cardiac tissue these events can be observed by using an optical mapping of intracellular calcium concentration. Moreover, in two-dimensional cardiac tissue we observed spiral waves (Figure 1.3 (d)). These spiral waves reenter the same region of cardiac tissues more than once [30]. The presence of spiral waves distorts the single coordinated electrical wave that characterizes the sinus rhythm, thus, creating an ineffective electrical activity and contraction. As a result, this rapidly disorganizes ventricular contraction and causes VF. In

the case of VF, the spiral waves appear chaotically in different regions by a creation and annihilation process and the ECG recording shows chaotically oscillations (Figure 1.3 (e)) [26,30].

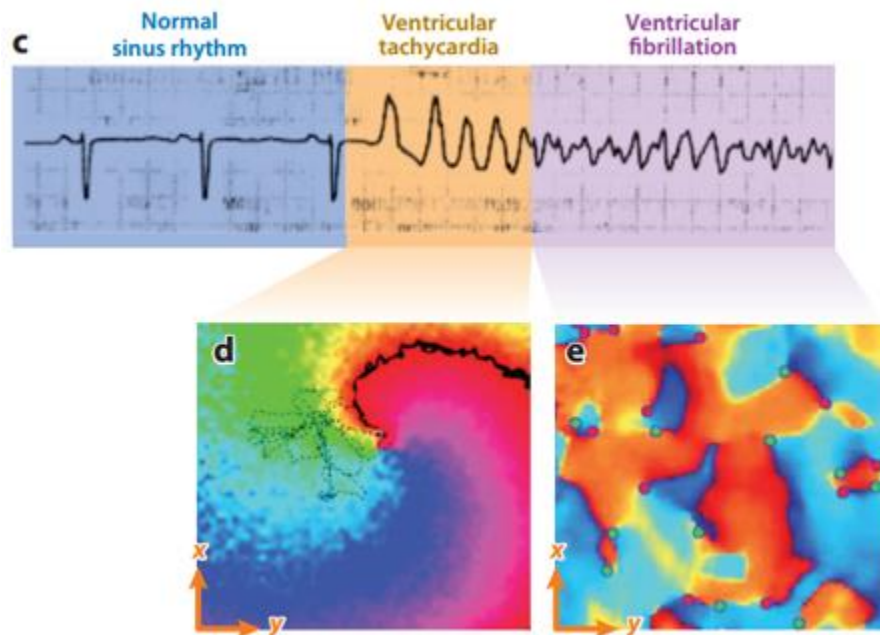


Figure 1.3 (c) ECG of a patient undergoing sudden cardiac arrest. (d) During ventricular tachycardia, a spiral wave is formed (image of a two-dimensional cardiac tissue). (e) In the regime of ventricular fibrillation wave turbulence occurs [30].

1.4 Cardiac arrhythmias initiation

Despite intensive research over the last two decades, the underlying mechanism leading to VF is not completely understood. The fundamental question is what is the mechanism that initiates the abrupt change in the sinus rhythm (Figure 1.4, red arrow)? **The abrupt change in the sinus rhythm as seen in the ECG is believed to be initiated by triggered activity. Triggered activity can prompt excitations (ectopic foci) wave fronts that can break to form reentrant electrical propagation that can initiate ventricular tachycardias [11].**

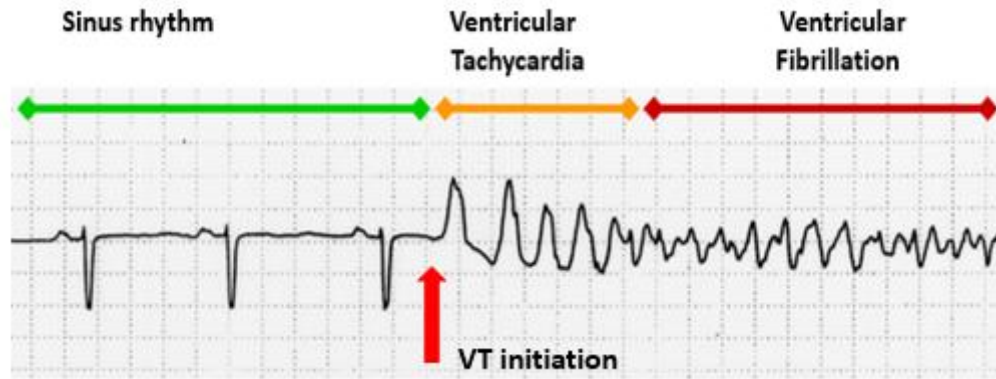


Figure 1.4 1 ECG recording showing the breakdown of the electrical rhythm. The event leading to ventricular tachycardia is emphasized.

Calcium (Ca) can be released from the sarcoplasmic reticulum via ryanodine receptors (RyRs) independently of Ca influx from voltage-dependent membrane channels. This fluctuations in the RyRs can produce a calcium overload. The calcium overload in this process is referred to as spontaneous Ca release (SCR) which can induce spontaneous sparks and propagate to form spontaneous Ca waves [4]. It is believed that spontaneous Ca waves can cause the sodium/calcium exchanger to induce abnormal currents into the membrane potential that produce delayed afterdepolarizations (DADs) [26]. Figure 1.5 (A) illustrates the membrane potential (V_m) and Ca transients of an experiment from a site near the endocardium. During endocardium rapid pacing spontaneous calcium release produces a DAD, thus, creating an ectopic beat (asterisk). This ectopic beats are called triggered activity because they can generate repetitive propagated action potentials and initiate tachycardias [6, 11, 26].

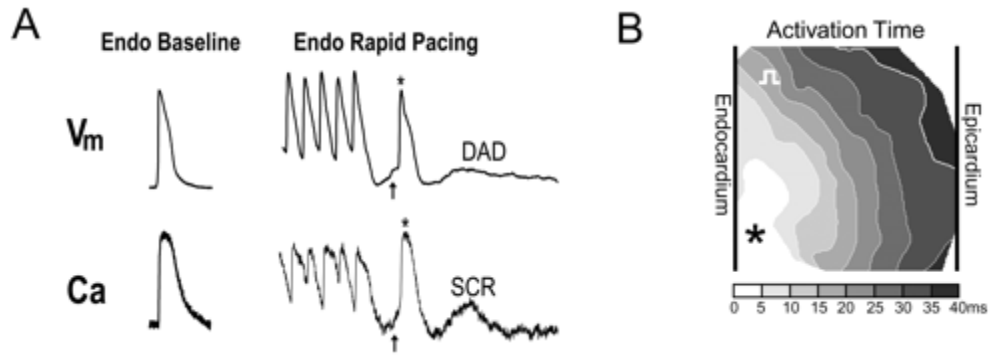


Figure 1.5 Triggered activity during calcium overload. (A) Representative action potential and calcium transients recording from endocardium baseline (right) followed by an abrupt halt in pacing (left). After rapid pacing an ectopic beat is evident (*). (B) Shows the origin of the ectopic beat close to the endocardium but away from the site of stimulation [8].

Since triggered activity is associated to spontaneous calcium release, an understanding of subcellular Ca is necessary. However, to date, there is no mathematical model of SCR that accounts for experimentally observed features of subcellular Ca. By introducing a simplified theoretical model, we found an explanation to the essential features of Ca waves such as nucleation and propagation. In addition, we now understand what determines the timing and location of spontaneous calcium waves within myocytes.

Chapter 2: Intracellular calcium release

2.1 Spontaneous calcium release

At the intracellular level, a central role is played by the Ryanodine receptor (RyR) which controls the flow of Ca from intracellular Ca stores to the cell interior. An important feature of RyR channels is that they are highly sensitive to Ca and transition from a closed to open state in a Ca dependent manner. This Ca sensitivity, which is mediated by multiple binding sites on the channel, is further amplified by the close arrangement of RyR channels into clusters of 10 – 100 RyR channels[2]. This architecture ensures that small increases of local Ca concentration can trigger a domino like opening of an array of RyR channels, leading to a large local release of Ca[3]. In a cardiac cell there are several thousand of these clusters organized along equally spaced planes (Z-planes), so that signaling is determined by the number and timing of these release events. This signaling architecture is found in a wide variety of cell types and is utilized to control the spatiotemporal distribution of Ca in the cell (Figure 2.1) [1].

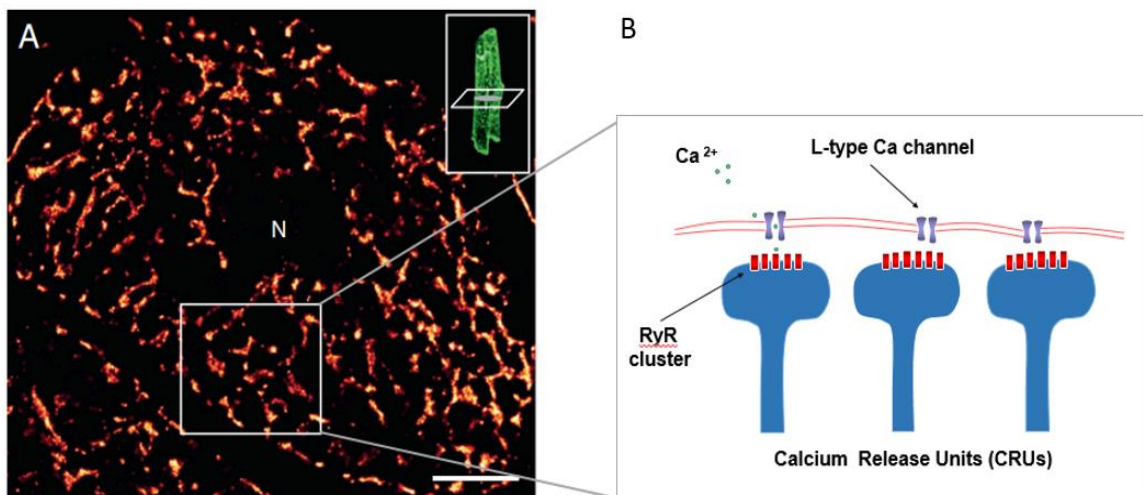


Figure 2.1 (A) RyR distribution in rat ventricular myocytes. Pseudocolour transverse (super-resolution microscopy) image at the z-planes of a myocyte [27]. (B) RyR clusters forming the calcium release units (CRUs).

Under normal conditions RyR channels are stimulated by the opening of voltage gated L-type Ca channels (LCC) which release the needed local concentration. However, sometimes the nonlinear response of RyR receptors in clusters responds abnormally and release extra amounts of calcium. If there is a calcium overload, calcium at a given cluster can diffuse and activate its nearest neighbors. Experimental studies have shown that there exist a hierarchy of abnormal Ca activation of its nearest neighbors. This hierarchy ranges from small to large events; Ca quark, sparks, abortive macrosparks and finally full waves [15].

Calcium overload can produce quarks, sparks, macro-sparks and under extreme conditions can cause a fire-diffuse-fire wave like in Figure 2.2 that can propagate in the cell [4-6]. These Ca propagation events are referred to as spontaneous Ca release since the release that occurs in this fashion is typically initiated by a random opening of a single or group of RyR clusters[4].

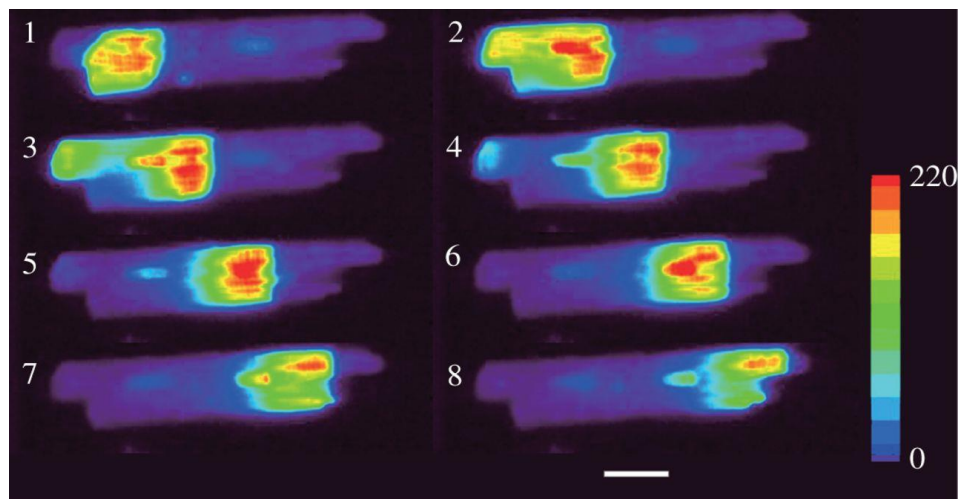


Figure 2.2 Experimental snapshots (100 ms apart) of a calcium wave initiating from the boundary of a cardiac myocytes. Scale bar, 20 μm [29].

2.2 Studies of spontaneous calcium release

Experimental and theoretical studies reveal a wide range of complex spatiotemporal dynamics of Ca depending upon physiological conditions and cell type [12-16]. In particular Falcke et al. [12] studied stochastic spreading in an array of discrete sites and identified a non-propagating to propagating transition. Interestingly, the propagation dynamics could be described as a directed percolation process, and also as a depinning transition depending upon system parameters. More recently, Nivala et al. [15] performed numerical and experimental studies to explore the emergence of SCR as a function of SR load. These authors found that at low SR loads Ca sparks typically occur in the cell in a stochastic manner but rarely transition to Ca waves. However, as the SR load is increased Ca waves are nucleated in the cell interior with greater frequency; although the distance of propagation is small i.e. the waves tend to fail after propagating a distance of several micrometers. Further increases in SR load led to longer propagation distances until waves propagate the extent of the cell leading to a substantial release of Ca. In earlier work Marchant and Parker [17] used fluorescence imaging to analyze the nucleation of Ca waves in *Xenopus* oocytes. In these cells Ca release is governed by clusters of inositol (1,4,5)-triphosphate (IP3) receptors which mediate the flow of Ca in similar fashion as do RyRs in cardiac cells. They found that waves tend to nucleate at specific regions of the cell characterized by a higher density of release sites and sensitivity to stimulation. Furthermore, they noticed that when the period between Ca waves was long then wave

nucleation occurred at specific sites with greater reliability. While these studies shed light on various aspects of subcellular Ca dynamics, several questions remain unanswered.

2.3 A new model for the nucleation of calcium waves in cardiac cells

Despite a great deal of work the basic features of spontaneous Ca waves (SCR) are still not fully understood. For example, it is not known how the spatial distribution of CRUs dictates the location of wave nucleation sites in the cardiac cell. Here, we introduce a simplified theoretical model that can be used to understand essential features of Ca wave nucleation and propagation. We analyze in detail the role of the random arrangement of CRUs inside the cell, the strength of diffusive coupling, and the kinetics of spark activation and extinguishing. Our goal is to determine how these properties determine the location and timing of spontaneous Ca waves in cardiac cells.

Chapter 3: A simplified stochastic model of wave nucleation

3.1 Physiological connection

In Fig. 3.1 we illustrate the basic architecture of subcellular Ca signaling in cardiac cells. Here, RyR channels form clusters of 10 – 150 channels which are distributed in the cell along planar invaginations referred to as Z-planes. We will refer to each of these clusters as a Ca release unit (CRU). Along each Z-plane the distribution of CRUs is random with an average spacing in the range 100 – 500nm while the spacing between planes is in the range 1 – 2 μ m [17,18], so that there are roughly 100 RyR CRUs on a Z-plane and about 10^4 in the cell.

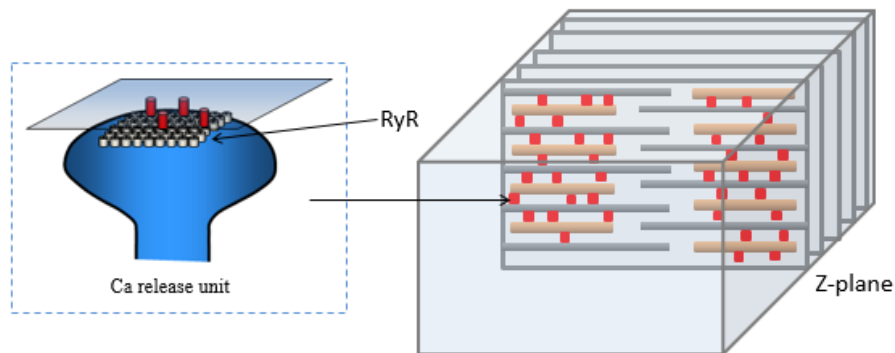


Figure 3.1. Illustration of the Ca signaling architecture. CRUs contain a few (1-5) LCC channels and a cluster (10-150) RyR channels responsible for Ca signaling. In ventricular myocytes CRUs are distributed along roughly 50 – 100 Z-planes with \sim 100 CRUs within each plane.

Under normal conditions RyR channels are stimulated by the opening of voltage gated L-type Ca channels (LCC) which raise the local concentration. However, under conditions of Ca overload fluctuations of RyR channels from the closed to the open state can induce spontaneous Ca sparks. In this case an RyR channel opening leads to a local increase in Ca which can diffuse and induce additional openings of the channels in the cluster. This

process is highly nonlinear and leads to a substantial increase of local Ca which can, in some cases, diffuse and stimulate nearest neighbors CRUs. When this occurs a Ca wave can be nucleated which can spread across the cell and induce a substantial release of Ca. It is these release events which are believed to underlie various cardiac arrhythmias.

3.2 The model

In this study we will apply a minimal model in order to explore the relationship between the arrangement of CRUs and the nucleation of Ca waves. Given the complexity of the local RyR kinetics in a cluster we will simplify the system by modeling the i^{th} CRU using a state variable η_i , which can be $\eta_i = 0$ (no spark) or $\eta_i = 1$ (spark). To model the stochastic dynamics of Ca sparks we let the state variable obey the reaction scheme



where α_i is the rate at which sparks are ignited at site i , and where β_i is the rate that a spark at that site is extinguished. Since, RyR cluster openings are regulated by the local Ca concentration then we will take the forward rate to be $\alpha_i = g_i c_i^\gamma$, where c_i is the local Ca concentration at site i , g_i represents the excitability of that CRU, and where γ is an exponent that describes the nonlinear dependence of the spark activation rate on the local Ca concentration. Experimental studies reveal that the open probability of RyR channels is a nonlinear sigmoid function of the local Ca concentration [3,19]. Thus, given the Ca mediated cooperativity between RyR channels in the cluster, we expect that the rate of spark formation should have a highly nonlinear dependence on the local Ca concentration. To account for this nonlinearity we will set $\gamma = 2$ in this study. Furthermore, we note that

in the cell Ca sparks terminate due to inactivation or SR depletion. Here, we focus only the dynamics of wave nucleation, and neglect the role of slow recovery processes due to a previous excitation.

In this study we will focus on spontaneous Ca waves that occur due to RyR channel openings and so we will consider the case where the LCC channels are shut. In this case the local Ca concentration at a CRU is given by

$$c_i = c_o + \sum_{j \neq i} h_{ij} \eta_j \quad (2)$$

where c_o is the background Ca concentration, and where h_{ij} gives the rise in the local Ca concentration at site i due to an active Ca spark at site j ($\eta_j = 1$). To model interactions between CRUs we note that the solution of the diffusion equation in an isotropic medium requires that the concentration at site i due to Ca released at site j should fall off as $\sim \exp(-d_{ij}^2/l_{ij}^2)$. Here, d_{ij} is the distance between the CRUs, and l_{ij} is a diffusive length scale that is determined by the diffusion coefficient of Ca in the intracellular space between sites i and j , and also the lifetime of the Ca spark at site j . To model this effect we will consider coupling between CRUs of the form

$$h_{ij} = r_j \exp \left[-|\vec{x}_i - \vec{x}_j|^2 / l_{ij}^2 \right], \quad (3)$$

Where r_j represents the Ca released at site j , \vec{x}_i and \vec{x}_j are the location of the i^{th} and j^{th} CRUs in the cell.

3.3 System parameters

To model the spatial distribution of active sparks in a cell we will consider the time evolution of our system in two dimensions (2D). Thus, we consider the dynamics of N CRUs that are placed at random locations on a square of size $L \times L$. This arrangement introduces a length scale which is the average minimum distance between CRUs. This distance can be estimated to be $d \sim L/2\sqrt{N}$, so that a natural dimensionless parameter that characterizes the system is the ratio $s = l/d = 2\sqrt{N} l/L$, which gives a measure of the length scale of diffusive interactions compared to the average CRU spacing. Hereafter, we will refer to the parameter s as the spatial coupling strength. In this study we will consider the case where each CRU is equivalent so that $\alpha_i = \alpha, \beta_i = \beta, g_i = g$ and $r_i = r$. Also, we take the diffusive length scale to be a constant so that $l_{ij} = l$, so that the heterogeneity in the system originates only from the spatial arrangement of CRUs on the plane. The parameter r will be referred to as the excitability of the system since it gives a measure of the amount of Ca released at a CRU. To fix system parameters we will rely on existing experimental observations of Ca sparks and waves. Firstly, we will assume that Ca can diffuse between nearest neighbors depending on the amount of Ca released at each CRU. At high SR loads we expect that Ca released at a CRU can diffuse to several nearest neighbors so that we will consider spatial coupling in the range $0 < s < 6$. Also, we will also take $c_o = 0.01\mu M$ and let the spark rate of an isolated CRU to be $\alpha \sim 0.001 (ms)^{-1}$, which is roughly 1 spark every second. Since $\alpha = gc_o^2$ this will fix $g = 0.5(ms^{-1}\mu M^{-2})$. Finally, we note that since a Ca spark typically lasts for a duration 20 – 50ms we will take $\beta = 0.05 (ms^{-1})$.

3.4 System spatiotemporal dynamics

In Fig. 3.2A-C we show the spatiotemporal evolution of active sites starting with initial conditions such that all sites are inactive ($\eta_i = 0$). Our numerical simulations reveal that there are two distinct phases of the system. In one case, illustrated by Fig. 3.2A, Ca sparks are nucleated at localized regions of the system and proceed to spread rapidly as an advancing front of active sites, with $\eta_i = 1$, which invades the surrounding inactive region with $\eta_i = 0$. In Fig. 3.2A we show the spatial distribution of active sites for a short time interval following nucleation of the advancing front. In this regime the total number of active sites, denoted as $n(t)$, increases rapidly once a wave is nucleated (Fig. 3.2D, red trace), and the system settles to a final steady state where most of the sites are in the active state. In the case where the excitability and coupling are reduced we see that waves are not nucleated in the system (Fig. 3.2B). Here, the system slowly evolves towards a state where active sites form a sparse random pattern, where each unit fluctuates with time according to the local stochastic dynamics. In this case, the evolution of the spatial pattern does not occur via a coherent activation front but rather in a gradual fashion where the pattern of activity spreads in a diffuse manner. In this case we find that the number of active sites increases on a much slower time scale (Fig. 3.2D, blue trace). As the coupling is reduced further (Fig. 3.2C) the spreading of active sites occurs even more slowly, and settles in a sparse random pattern where only a few sites are active. Here, we find that the steady state is governed by clumps of active sites spread randomly throughout the system. These distinct cases are representative of the possible spatiotemporal evolution of the system.

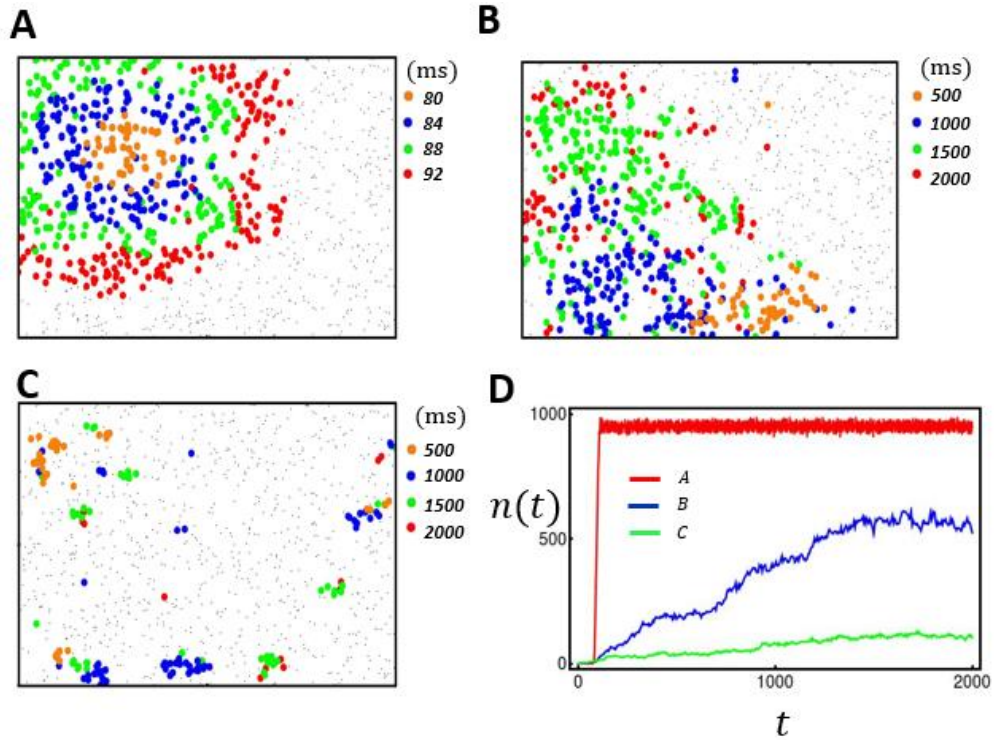


Figure 3.2 Spatiotemporal dynamics. Spatiotemporal evolution of active sites in a system with $N=1000$ CRUs and $L=1$. (A) Ca sparks are nucleated at localized regions and spread rapidly as an advancing front of active sites. In this case system parameters are chosen to be $s=4$ and $r=0.3$. Snap shots of active sites at the times shown are indicated. (B) For reduced excitability and coupling ($s=3, r=0.1$) active sites spread in a diffuse manner and settle in a disordered fluctuating pattern. (C) When the coupling is further reduced only a few sites are activated and randomly distributed in clumps in the system ($s=1, r=0.8$). (D) The total number of active sites $n(t)$ as a function of time for the three cases shown in A-C.

3.5 Timing and propagation of Ca waves

An important feature of the spatiotemporal dynamics is the nucleation of propagating Ca waves. To analyze the dynamics of waves we study the evolution of a front in 2D that joins a region of high activity with $\eta_i = 1$ with an inactive region with $\eta_i = 0$. Our goal is to determine the conditions for which the planar front advances in our system. To investigate this transition in the most simple setting we chose initial conditions such that

all points on our $L \times L$ square with $x \leq L/2$ are set to the value $\eta_i = 1$, and all points $x > L/2$ are $\eta_i = 0$ (Fig. 3.3A). To track the evolution of the front we average η_i in the y direction in bins of size $\Delta x = 1/40$ along the x axis. In Fig. 3.3B we show the time evolution of this projection showing that fronts can propagate from the active to inactive state. Analysis of these fronts reveals that for a given excitability r there is a critical coupling s_w ,

which we will refer to as the front propagation threshold, such that fronts will propagate with $s > s_w$ but remain pinned for $s < s_w$. In Fig. 3.3C we plot the function $s_w(r)$ which separates the propagating and non-propagating regions of phase space.

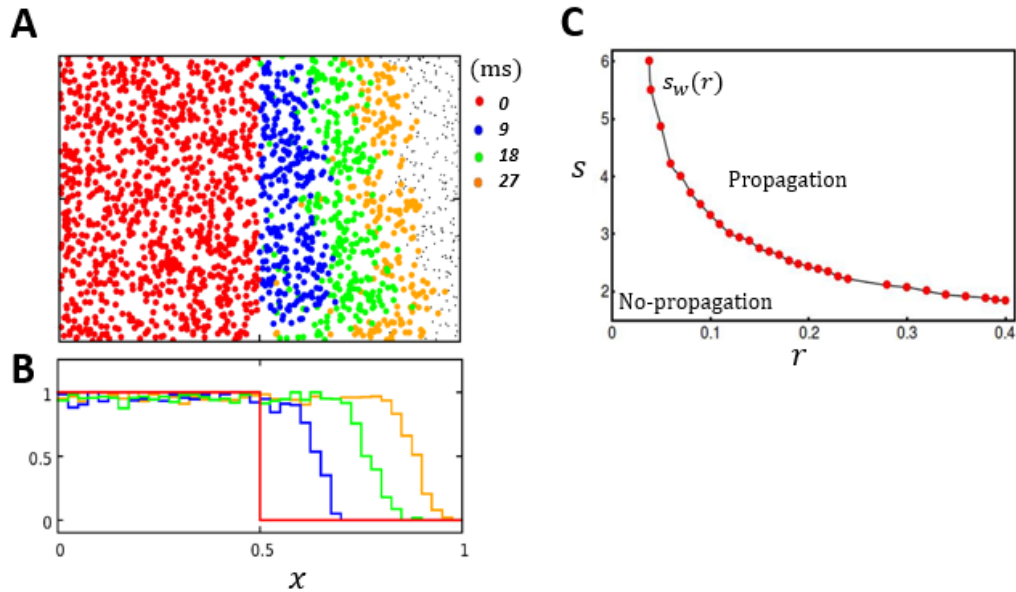


Figure 3.3. Front propagation and phase space. (A) The evolution of a planar front of active sites. Initial conditions are chosen such that $\eta_i = 1$ for $x < 1/2$ and $\eta_i = 0$ for $x > 1/2$ (red circles). System parameters are $s = 4$ and $r = 0.2$. (B) Evolution of wave front is tracked by averaging η_i in the y -direction in bins of size $\Delta x = 1/40$. Front evolution is shown for times $t = 0, 9, 18, 27$ ms. (C) Wave propagation threshold in parameter space.

To characterize the timing of wave nucleation we chose initial conditions so that all sites are inactive ($\eta_i = 0$), and determine the average waiting time T for a Ca wave to be nucleated in the system. Our criteria for wave nucleation is that the fraction of active sites exceeds 80% of the total number of CRUs in the system. In Fig. 3.4 we plot the average wave nucleation time, averaged over 100 independent simulations, as a function of the system excitability r , and for a range of values of the spatial coupling s . This result reveals that as the excitability r is reduced the wave nucleation time increases substantially. In our simulations we find that as r approaches the propagation threshold the first passage time T appears to diverge. In practice, simulation times become exceedingly large and we show results only up to a mean waiting time of $T = 1000ms$.

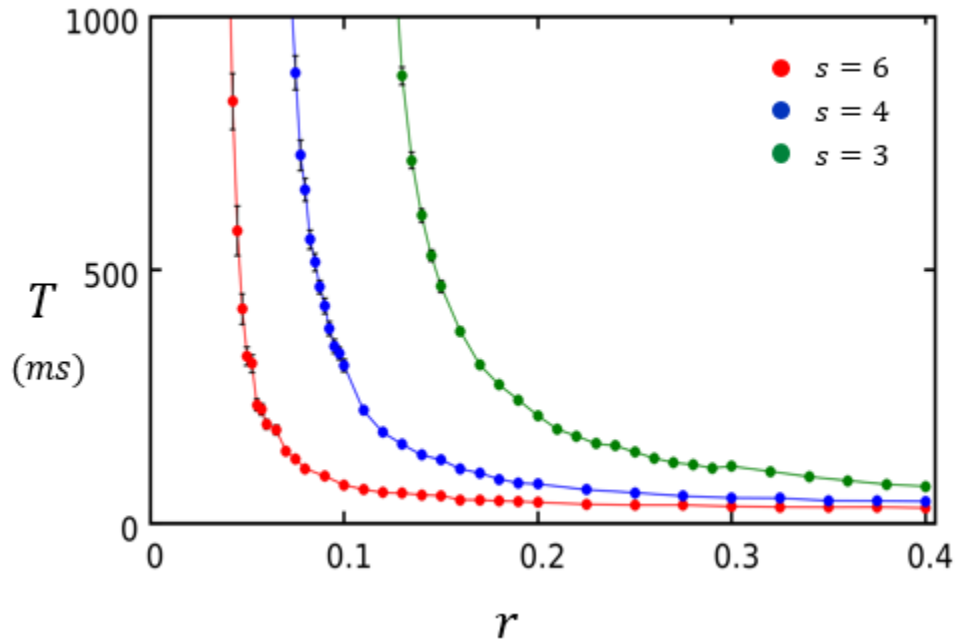


Figure 3.4. The average wave nucleation time, averaged over 100 independent simulations as a function of the system excitability r and spatial coupling $s = 3$ (green), $s = 4$ (blue), and $s = 6$ (red).

3.6 Steady state dynamics

To further characterize the system we have computed the long time dynamics of active sites. Thus, we compute the time dependence of the average number of active sites, which we define as $\langle \eta(t) \rangle = (1/N) \sum_{i=1}^N \eta_i$. Since the steady state dynamics depends crucially on initial conditions we will consider the dynamics of $\langle \eta(t) \rangle$ for broad range of initial conditions. Thus, we consider initial conditions so that the probability that a site is active ($\eta_i = 1$) is taken to have probability p , and where p will be varied in the range 0 to 1. In Fig. 3.5A-C we show the time evolution of $\langle \eta \rangle$ for a range of excitability r , and where the coupling is fixed at $s = 4$. Based on these simulations we identify three distinct steady state behaviors. For small values of r we find that the system evolves towards a low activity state where $\langle \eta \rangle \sim 0$ (Fig. 3.5A), independently of initial conditions. As r is increased further we find that $\langle \eta \rangle$ evolves towards multiple values depending upon the initial conditions (Fig. 3.5B). Hereafter, we will refer to this regime as the multistable phase. Finally, for larger r values the system again evolves to a state where $\langle \eta \rangle \sim 1$ independently of initial conditions (Fig. 3.5C).

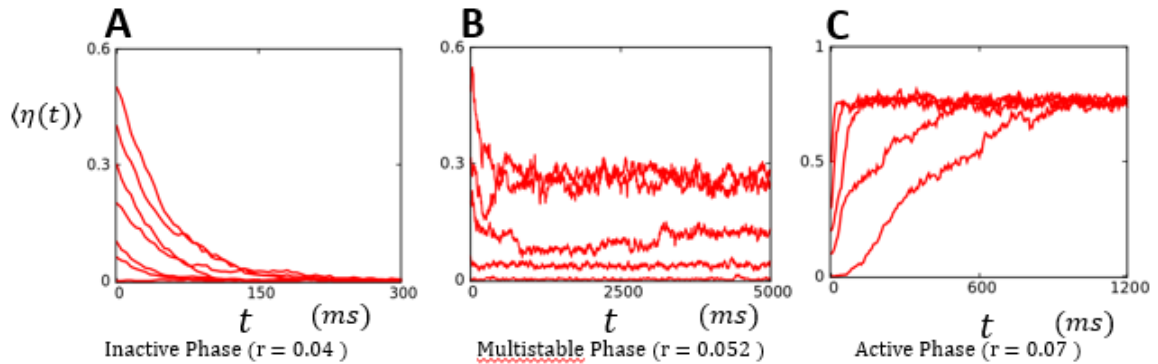


Figure 3.5. The average activity $\langle \eta(t) \rangle$ vs time for a range of initial conditions. Initial conditions are chosen so that (0,2,4,6,8,10,20,30,40,50) percent of the sites are active at

time $t = 0$. (A) Inactive phase with $r = 0.04$. (B) Multistable phase with $r = 0.052$. (C) Active phase with $r = 0.07$. In all cases coupling is set to $s = 4$.

To further quantify this behavior, in Fig. 3.6 we plot the value of $\langle \eta \rangle$ after a time of $t = 5000ms$, for a range of initial conditions. We have taken the value at this time since it is much longer than the transient dynamics observed, and the system appears to have reached steady state. Indeed, we find that for a range of excitabilities ($r_a < r < r_b$) $\langle \eta \rangle$ can attain several distinct values, while outside this range $\langle \eta \rangle \sim 0$ for $r < r_a$ and $\langle \eta \rangle \sim 1$ for $r > r_b$.

To quantify this finding we have also computed the variance σ of the steady state value of $\langle \eta \rangle$. Hence, we compute $\sigma = \sqrt{\overline{\langle \eta \rangle^2} - \overline{\langle \eta \rangle}^2}$, where \bar{x} denotes the sample average of x over the 10 initial conditions. As shown in Fig. 3.6 (red line) the variance σ increases substantially in the multistable phase of the system ($r_a < r < r_b$).

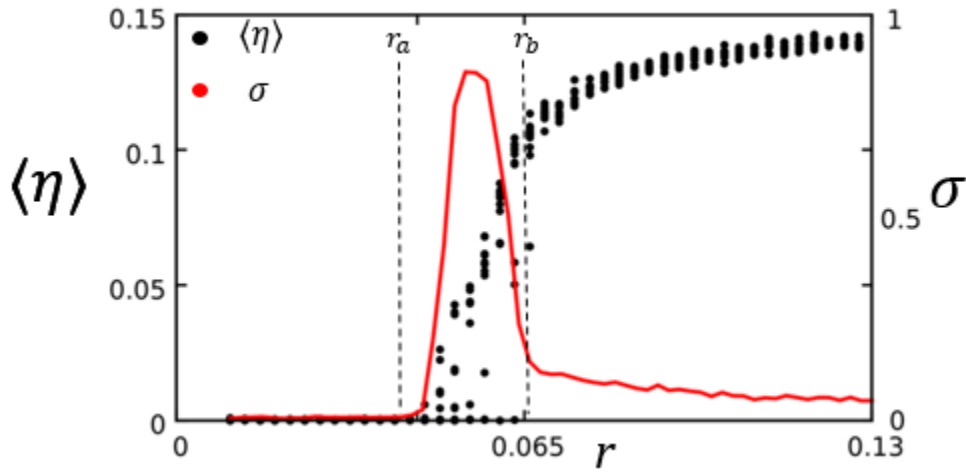


Figure 3.6 Plot of $\langle \eta \rangle$ at time $t = 5000ms$ (black circles) as a function of r . For each parameter value the system is simulated for the 10 initial conditions. Using the same data the variance σ is computed (red line).

Our simulations indicate that above the wave propagation threshold the system evolves towards the active state where $\langle \eta \rangle \sim 1$. Thus, we expect that the transition from the active to multistable phase, at $r = r_b$, should coincide with the wave propagation threshold. To check this hypothesis we have compared the wave propagation threshold to the onset of the multistable phase. To determine the onset of the multistable phase we note that the variance σ rises as r is decreased to $r = r_b$.

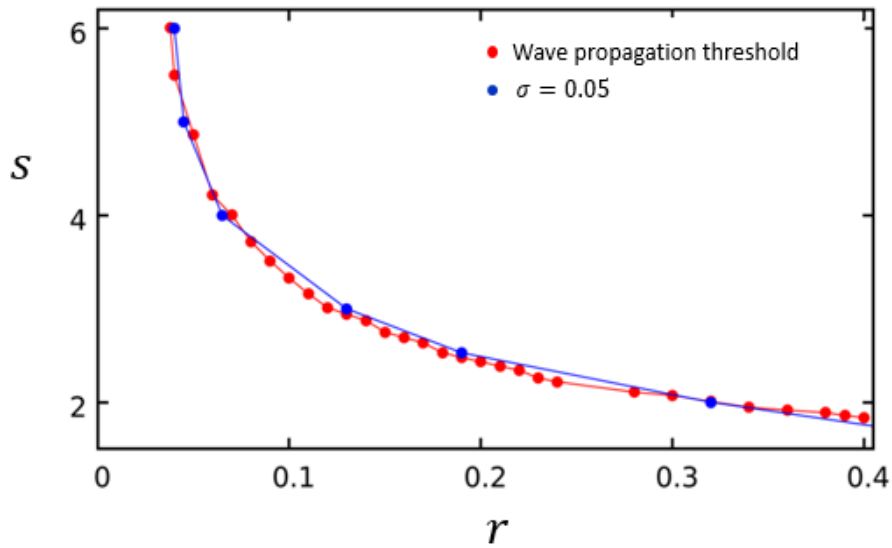


Figure 3.7. The wave propagation threshold (red line) and the transition line separating the monostable active and the multistable phase. The onset of the multistable phase is determined by finding the parameter r where the variance σ just exceeds 0.05.

Thus, an accurate marker for the onset of multistability is the value of r such that the variance has risen to the value $\sigma = 0.05$. In this way we can compute a quantitative estimate for the onset of the multistable phase. In Fig. 3.7 we have plotted the onset of the multistable phase along with the wave propagation threshold. Indeed, we find that these two lines are very close to each other. This result indicates that, as expected

intuitively, the onset of the multistable phase coincides with the threshold for wave propagation.

Chapter 4: A deterministic model of wave nucleation initiation

4.1 Deterministic mean-field theory

The numerical simulations of our stochastic spark model reveal rich spatiotemporal properties. In order to understand basic features of the system we develop a simplified mean field theory which will shed light on various aspects of the dynamics. Let us first define the spark probability $P_i(t)$ to be the probability that the i^{th} CRU is active ($\eta_i(t) = 1$) at time t . The stochastic dynamics is then governed by the master equation

$$P_i(t + \tau) = (1 - P_i(t))(\alpha_i\tau) + P_i(t)(1 - \beta_i\tau) \quad (4)$$

where $\alpha_i\tau$ and $\beta_i\tau$ are the transition probability that site i makes a $0 \rightarrow 1$ or $1 \rightarrow 0$ transition in the time interval τ . To simplify the dynamics we will make the approximation that the state variables can be replaced by their averages so that $\eta_j \approx P_j$, and the local Ca concentration can be approximated by $c_i \approx c_o + \sum_{j \neq i} h_{ij} P_j(t)$. In the continuum limit the master equation then simplifies to the system of equations

$$\frac{dP_i}{dt} = g_i \left(c_o + \sum_{j \neq i} h_{ij} P_j \right)^2 (1 - P_i) - \beta_i P_i, \quad (5)$$

which describes the time evolution of the spark probability $P_i(t)$.

4.2 Steady state dynamics of mean-field theory

To analyze the dynamics of the mean field equations we first consider steady state solutions to the N nonlinear equations given in Eq. 5. To distinguish steady state solutions we keep track of the average site probability defined here as $\langle P(t) \rangle = (1/N) \sum_{i=1}^N P_i(t)$,

and denote the steady state occupation probability as $\langle P \rangle_\infty = \langle P(t \rightarrow \infty) \rangle$. To capture the system behavior over a wide range of parameters we will compute $\langle P \rangle_\infty$ vs the excitability r , for different values of the dimensionless ratio s . As in the full stochastic model Eq. 5 can have multiple steady state solutions, which can be reached depending upon the initial conditions chosen. Thus, we consider a range of initial conditions of the form $P_i = p + \xi_i$, where p is an average that will be varied, and where ξ_i is a uniformly distributed random number with an average $\langle \xi \rangle \ll p$. By considering the time evolution of an ensemble of initial conditions, with varying p and $\langle \xi \rangle$, we can then explore the possible steady state solutions to Eq. 5. Our main results are summarized in Fig. 4.1 where we have plotted $\langle P \rangle_\infty$ vs r for a fixed coupling of $s = 3$.

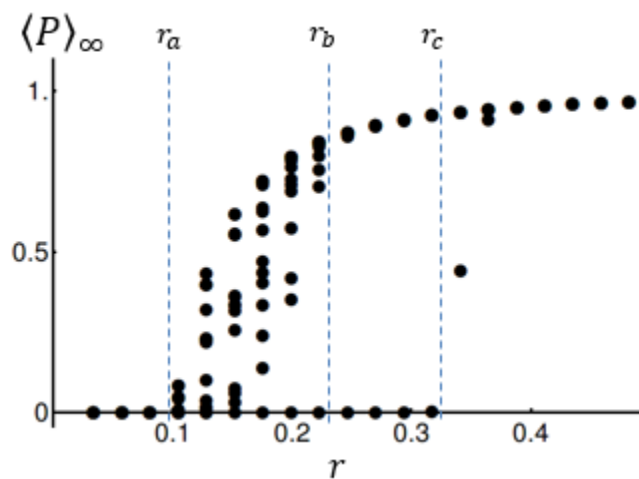


Figure 4.1 Dynamics of the mean field theory. Steady state average site probability $\langle P \rangle_\infty$ vs r computed for randomly chosen initial conditions. In this simulation the coupling parameter is fixed at $s = 3$ and steady state is taken to be the solution at time $t = 1000ms$. The number of sites is taken to be $N = 500$ and the ODEs are integrated with a time step of $dt = 0.01ms$.

We find that for $r < r_a$ then there is effectively only one steady state solution vector P_i with $\langle P \rangle_\infty \sim 0$ [Fig. 4.2(a)]. This solution corresponds to the inactive state of the system

where the steady state probability of active sites is low. For larger excitability r we find that there is a region of parameter space between r_a and r_b where there are multiple steady state solutions which can be reached depending upon the initial conditions [Fig 4.2(b)]. However, for larger excitability ($r_b < r < r_c$) we find that these multiple states collapse into effectively two distinct solutions. In this regime the system is bistable and can be either in the active state ($\langle P \rangle_\infty \sim 1$) where most sites are active, or the inactive state where the system is quiescent ($\langle P \rangle_\infty \sim 0$) [Fig. 4.2 (c)]. For even larger excitability $r > r_c$ the lower branch vanishes and the system evolves to a single unique solution in which $\langle P \rangle_\infty \sim 1$ [Fig. 4.2(d)].

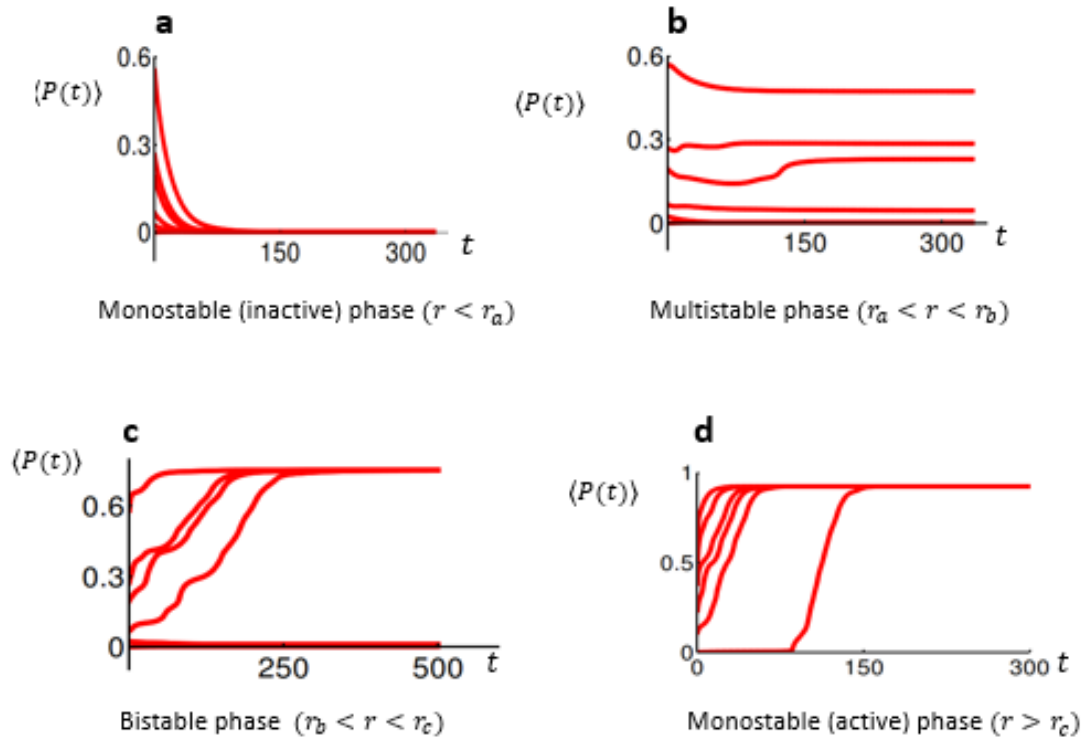


Figure 4.2. (a-d) Sample traces of $\langle P(t) \rangle$ vs time t showing evolution to (a) mono-stable inactive, (b) multi-stable (c) bistable (d) mono-stable active phase.

In order to characterize the steady state behavior of the mean field equations we have constructed the full phase diagram of the mean field theory. In Fig. 4.3 we plot the boundaries separating the monostable, bistable, and multistable phases of the mean field equations. As in the full stochastic model we find that the mean field equations also possess propagating front solutions. To investigate the wave propagation threshold we simulate the time evolution of a planar front in 2D which joins the active ($P_i = 1$) and quiescent state ($P_i = 0$).

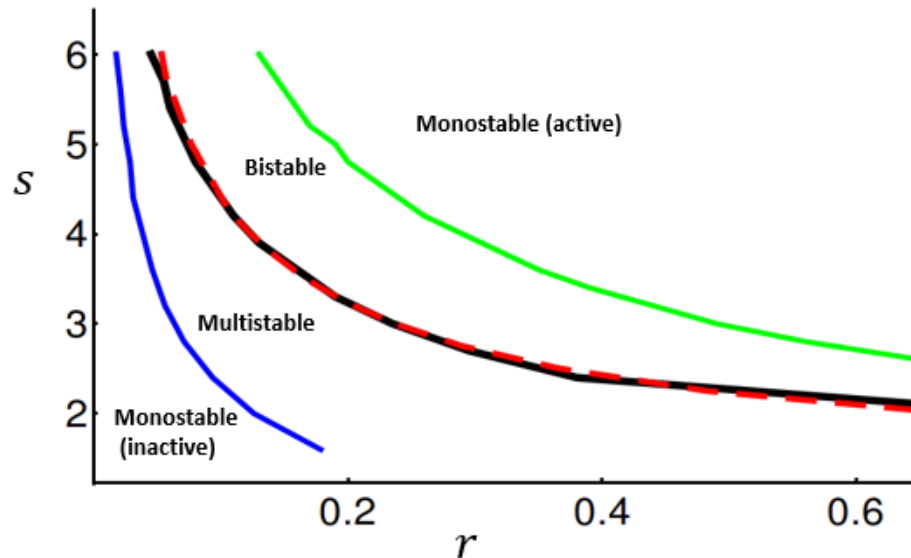


Fig. 4.3 Phase diagram of the mean field equations showing the phase boundaries between the indicated states.

4.3 Role of fluctuations

A basic limitation of the mean field theory is that it neglects fluctuations. Thus, key features of the full stochastic model, such as stochastic wave nucleation, cannot be described in this picture. To investigate the role of fluctuations we will introduce a noise term to Eq. 5. Thus, we will consider equations of the form

$$\frac{dP_i}{dt} = g_i \left(c_o + \sum_{j \neq i} s_{ij} P_j \right)^2 (1 - P_i) - \beta_i P_i + \xi_i(t), \quad (6)$$

where $\xi_i(t)$ is a Gaussian noise term that satisfies $\langle \xi_i(t) \xi_j(t') \rangle = D^2 \delta_{ij} \delta(t - t')$, and where $\langle \xi_i(t) \rangle = 0$. In this scenario the deterministic equations are driven by uncorrelated noise which should mimic the effect of stochastic fluctuations from the reaction scheme given by Eq. 1. In this study we seek to explore the qualitative behavior of Eq. (6) and so we will consider the system behavior for a wide range of noise strengths. Thus we will choose our noise amplitude so that $D = \sqrt{\langle \xi^2 \rangle}$ is in the range $10^{-4} - 10^{-2}$. Eq. 6 is solved directly using a standard Euler scheme [20], where it is necessary to introduce a boundary condition that fluctuations cannot induce unphysical probabilities below zero. Thus, during the numerical time stepping we impose the condition that $P_i = 0$ when $P_i < 0$.

To explore the behavior of Eq. 6 we will compute the long time dynamics of the average probability $\langle P(t) \rangle$. Firstly, we note that the deterministic ODEs (Eq. 5) reach steady state in a time $t \sim 100ms$. Thus, we will approximate the steady state average probability to be $\langle P \rangle_\infty = \langle P(t = 1000ms) \rangle$. In Fig. 4.4A we show $\langle P \rangle_\infty$ vs r for a range of values of the noise amplitude D . We find that as D is increased, the range of excitability r , where bistability and multistability is observed, is substantially reduced. In particular, for $D = 10^{-2}$ the bistable regime is eliminated and the dispersion of the multistable phase is small. The reason for this decrease in dispersion is illustrated in Fig. 4.4B where we show the effect of noise on the temporal evolution of the system. In this simulation we have chosen $r = 0.16$ so that the deterministic system is in the multistable phase. For times $t < 800ms$

we set $D = 0$ and let the system evolve towards distinct steady state values depending upon the initial conditions. For times $t > 800ms$ we turn on noise so that $D = 10^{-2}$ and observe that $\langle P \rangle$ evolves towards a smaller set of steady state values. Here, we find that the steady state behavior attained in the deterministic limit is unstable to noise perturbations so that a new set of steady state values is attained once the noise is turned on. In Fig. 4.4C we plot the mean waiting time to wave nucleation when the noise amplitude is $D = 10^{-2}$. Indeed, consistent with our stochastic model (Fig. 3.4), we find that the mean waiting time diverges rapidly as the excitability is reduced towards the wave propagation threshold. These numerical results indicate that the mean-field equations with noise captures qualitative features of our stochastic system.

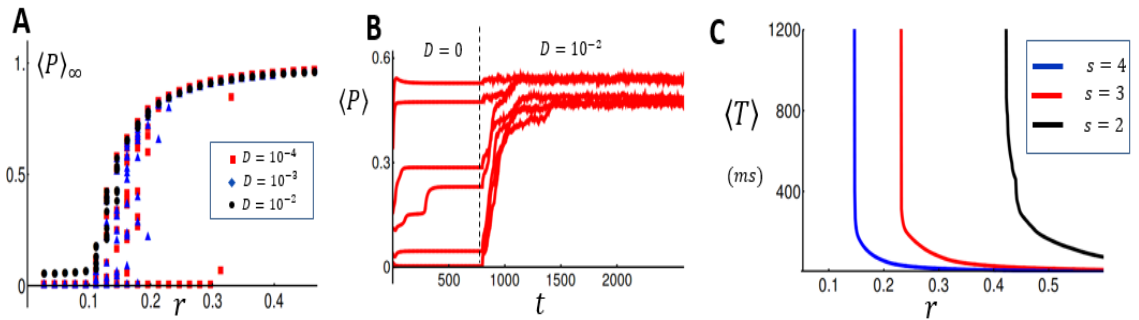


Figure 4.4. Properties of the mean field equations with noise. (A) Average site probability $\langle P \rangle_\infty$ vs r computed for 10 randomly chosen initial conditions. Here, $\langle P \rangle_\infty$ is taken to be the average site probability evaluated at time $t = 1000ms$. Noise strength is shown on the inset and spatial coupling is set to $s = 3$. ODEs are integrated using a time step of $dt = 0.01$. (B) Time dependence of $\langle P(t) \rangle$. At $t = 800ms$ noise strength is increased from $D = 0$ to $D = 10^{-2}$. Excitability is fixed at $r = 0.16$. (C) Mean first passage time to wave nucleation computed with the stochastic mean field equations. Noise strength is fixed at $D = 10^{-2}$.

4.4 Linear stability analysis

Our numerical analysis of the deterministic mean field equations (Eq. 5) reveals a complex phase diagram. A distinct feature of the system is that for large excitability $r > r_c$ the steady state solution with $P_i \approx 0$ becomes unstable, and the system always evolves towards the fully active state with $P_i \approx 1$. To analyze this transition we consider the stability of the $P_i \approx 0$ solution. In this case we expand Eq. 5 near the steady state solution p_i^* so that $P_i = p_i^* + u_i$, and where u_i is a small perturbation. Expanding to linear order in u_i gives the linear system of equations

$$\frac{du_i}{dt} = -(\beta_i + g_i (c_o + q_i)^2)u_i + 2g_i(1 - p_i^*)(c_o + q_i)v_i, \quad (7)$$

where $q_i = \sum_j h_{ij}p_j^*$, and where $v_i = \sum_j h_{ij}u_j$. Thus, the stability of the low activity state is dictated by the system of equations $\dot{u}_i = \sum_j Q_{ij}u_j$ where

$$Q_{ij} = -(\beta_i + g_i(c_o + q_i)^2)\delta_{ij} + 2g_i(1 - p_i^*)(c_o + q_i) h_{ij}, \quad (8)$$

The time evolution of the system is then given by

$$\vec{u}(t) = \sum_k a_k e^{\lambda_k t} \vec{\phi}_k, \quad (9)$$

where λ_k and ϕ_k are the eigenvalues and eigenvectors of the matrix Q_{ij} . Thus, the quiescent state is unstable when the maximum eigenvalue, which we denote here as λ_1 , satisfies the condition $\lambda_1 \geq 0$.

To simplify the analysis further we note that the steady state occupation probabilities are small so that $p_i^* \sim 0$, so that $1 - p_i^* \sim 1$. We will also assume that each site is identical so that $r_i = r$ and $g_i = g$. Finally, we will make the assumption that the terms $q_i = \sum_j h_{ij}p_j^*$ do not vary substantially from site to site. We have checked this assumption numerically

and find that site-to-site variations in q_i have little effect on the leading eigenvalues and eigenvectors of the matrix Q_{ij} . Hence, we will make the replacement $q_i \rightarrow \langle q \rangle$, where $\langle q \rangle = (1/N) \sum_i q_i$ is the site average. This gives an approximation

$$Q_{ij} \approx -(\beta + g(c_o + \langle q \rangle)^2) \delta_{ij} + 2gr(c_o + \langle q \rangle) C_{ij}, \quad (10)$$

where $C_{ij} = \exp[-|\vec{x}_i - \vec{x}_j|^2/l^2]$ is the connectivity matrix. The leading eigenvalue is given by $\lambda_1 = -(\beta + g(c_o + \langle q \rangle)^2) + 2gr(c_o + \langle q \rangle)\lambda_c$, where λ_c is the leading eigenvalue of the matrix C_{ij} , and where the spatial evolution of the system is governed by the eigenvector of the matrix C_{ij} which corresponds to λ_c .

Chapter 5: Network structure

5.1 Localization of eigenvectors

The linear stability analysis allows us to understand the spreading of activity from an initially low active state. According to Eq. 9 the initial spreading dynamics will be dictated by the eigenvectors which correspond to the largest eigenvalues of the connectivity matrix C_{ij} . Here, we will explore the spatial structure of these eigenvectors in order to determine the nucleation sites of Ca waves. To determine the shape of the leading eigenvector $\vec{\phi}_1$ we rescale the eigenvector components, denoted as ϕ_{1i} , so that the component with the maximum magnitude has the value 1. We then plot ϕ_{1i} vs i where the i^{th} component is that component with the i^{th} largest magnitude. The ordered magnitudes for a system of $N = 1000$ sites, and for different values of the coupling parameter s , are shown in Fig. 5.1A. This result indicates that eigenvector components are strongly peaked at a small fraction of sites in the system. In order to see the spatial distribution of the leading eigenvector we have also plotted all spatial sites with eigenvector components with magnitude $\phi_{1i} > 0.5$. In Fig.5.1B we show the spatial distribution of these sites for different values of the coupling parameter s . This result demonstrates that the eigenvectors of the connectivity matrix C_{ij} are localized at specific regions in the system.

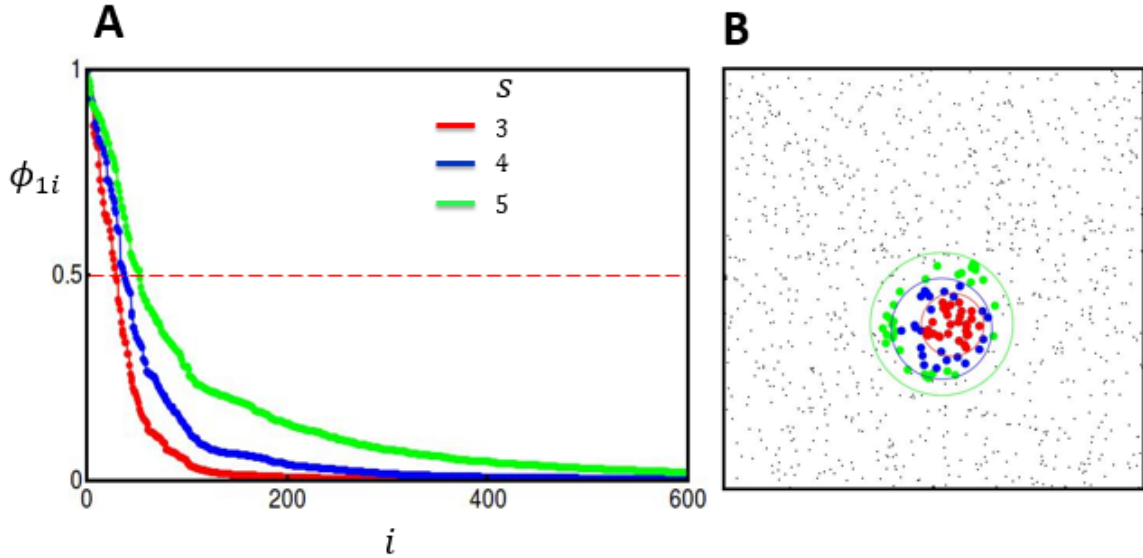


Figure 5.1 (A) Ordered components of the leading eigenvector $\vec{\phi}_1$, with elements normalized so that the maximum is one. The system size is taken to be $N = 1000$. (B) Eigenvector components with magnitude larger than 0.5 plotted in the space of points for $s = 3$ (red), $s = 4$ (blue) and $s = 5$ (green).

5.2 Stochastic and Deterministic prediction of wave nucleation

Our linear stability analysis reveals that the inactive state ($\eta_i = 0$) is unstable when $\lambda_1 > 0$, and that spreading will be localized on a few sites determined by the leading eigenvector $\vec{\phi}_1$. In this section we will proceed directly to the full stochastic model to determine the spatial distribution of localization sites. To determine these nucleation sites we simulate the stochastic evolution of the initially quiescent state and determine the spatial distribution of active sites at the onset of wave nucleation. To achieve this, our approach was to first determine the time t_a where the number of active sites reached 3% of the steady state number of active sites (n_∞) after wave nucleation. This simulation is repeated for M times, and for each site i in our system we compute the ratio $\rho_i = n_i(t_a)/M$, where $n_i(t_a)$ is the total number of instances when site i is active at the nucleation time t_a . Using this approach

we can construct the spatial density of active sites at the onset of wave nucleation. In Fig. 5.2A we show the spatial density of active sites in our system computed using $M = 20000$ simulation runs. In this simulation we find that most of the waves are nucleated at a specific localized region in the system (see density scale). In Fig. 5.2B we plot all sites with magnitude greater than 0.5 for the eigenvectors corresponding to the three largest eigenvalues. Indeed, we find that the localization area of these eigenvectors corresponds to sites where the density of nucleation sites is peaked.

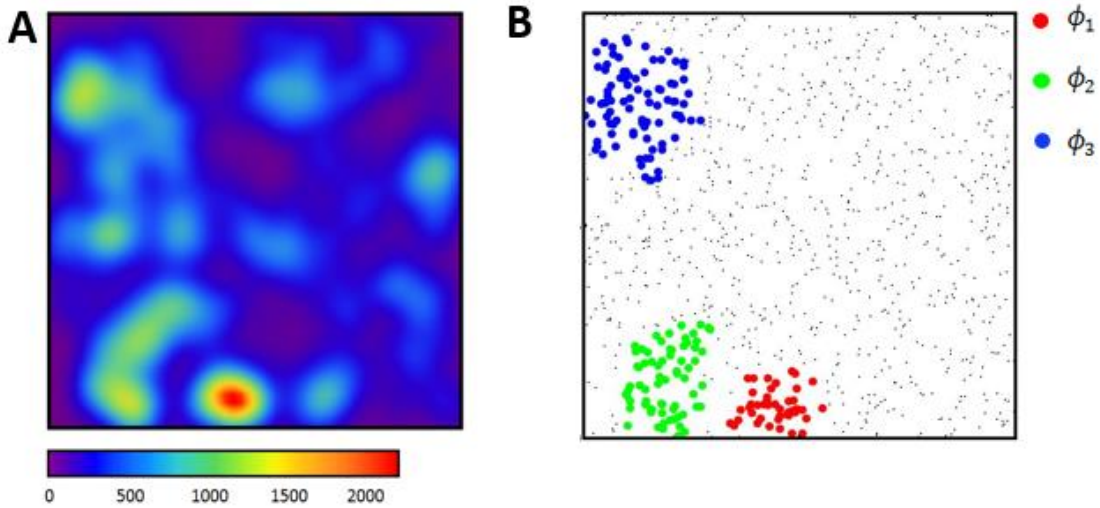


Figure 4.2 Density of nucleation sites and eigenvectors. (A) Spatial density of wave nucleation sites computed using 20,000 simulation runs. (B) Sites with magnitude $\phi_i > 0.5$ for the eigenvectors corresponding to the three highest eigenvalues.

Our numerical simulations reveal strong correlations between the leading eigenvectors of the connectivity matrix C_{ij} and the density of Ca wave nucleation sites. To check this prediction quantitatively we have computed the Pearson correlation coefficient between the leading eigenvector $\vec{\phi}_1$ and the density vector $\vec{\rho}$ at the onset of wave nucleation. To compare these two vectors we compute their similarity using the standard Pearson correlation coefficient which is given by the quantity

$$C(\vec{\rho}, \vec{\phi}_1) = \frac{\sum_i^N (\rho_i - \langle \rho \rangle)(\phi_{1i} - \langle \phi \rangle)}{\sqrt{\sum_i^N (\rho_i - \langle \rho \rangle)^2} \sqrt{\sum_i^N (\phi_{1i} - \langle \phi \rangle)^2}}, \quad (11)$$

so that $C(\vec{\rho}, \vec{\phi}_1) \sim 1$ or 0 if the vectors are strongly correlated or uncorrelated. In Fig. 5.3 we plot the correlation coefficient C vs. the excitability r showing that the correlation increases as the excitability is decreased towards the wave propagation threshold. This result demonstrates that the leading eigenvector of the connectivity matrix becomes increasingly predictive of the spatial distribution of wave nucleation sites as the system excitability is decreased.

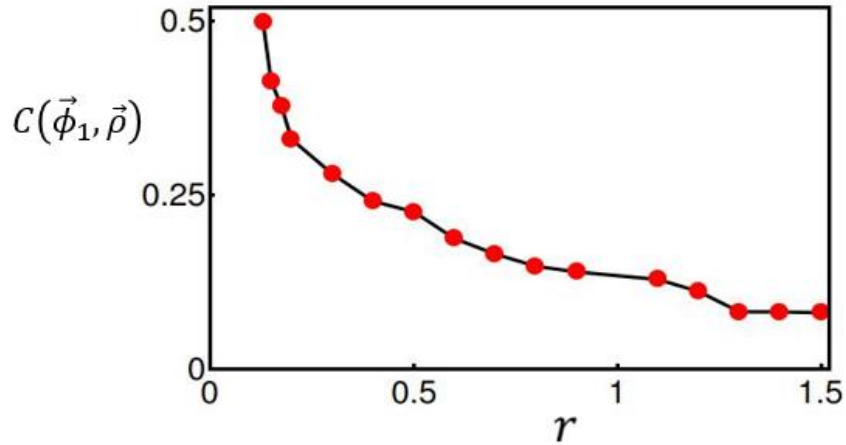


Figure 5.3 Pearson Correlation vs the excitability parameter r . Pearson correlation coefficient between nucleation density vector $\vec{\rho}$ and the largest eigenvector $\vec{\phi}_1$ plotted as a function of the excitability parameter r .

The relationship between the leading eigenvector and the nucleation site probability distribution should also hold in the mean field theory with noise (Eq. 6). To check this result we chose parameters above the wave propagation threshold, and consider the time evolution of a sparse initial pattern with $\langle P \rangle \sim 0$. In this parameter regime we measure the time t_a when the average site probability has increased to $\langle P(t_a) \rangle = 0.1$. We then

compute the Pearson correlation $C(\vec{P}(t_a), \vec{\phi}_1)$ where $\vec{P}(t_a)$ is the probability of release sites at the onset of wave nucleation. In Fig. 5.4 we plot C vs r , which shows that the correlation increases as the excitability r is decreased. On the same graph we overlay the steady state average $\langle P \rangle_\infty$ computed using the deterministic mean field theory. Here, we note that the leading eigenvector is predictive of the wave initiation sites for $r < r_c$, which is the regime in which the leading eigenvector is stable ($\lambda_1 < 0$). These results indicate that the leading eigenvector is predictive up to the wave propagation threshold.

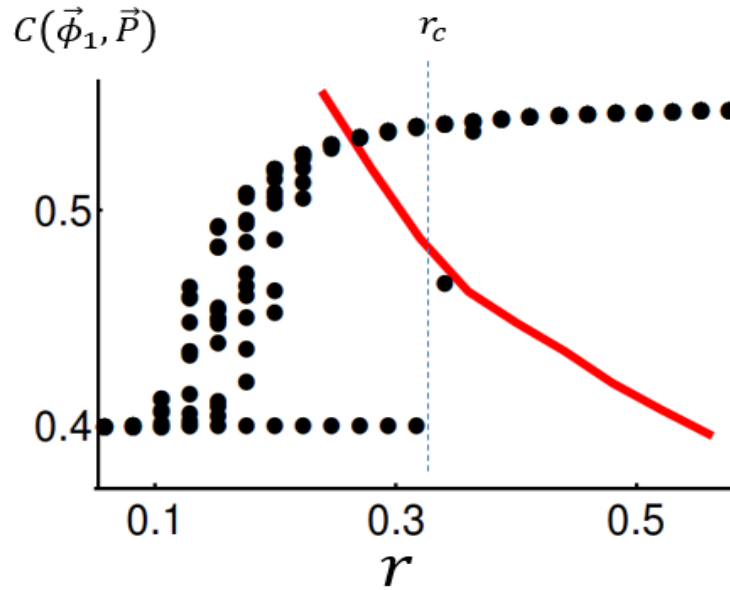


Figure 4.4 . The Pearson correlation between the leading eigenvector $\vec{\phi}_1$ and the site probability. (A) The Pearson correlation between the leading eigenvector $\vec{\phi}_1$ and the site probability $\vec{P}(t_a)$ taken at a time t_a where $\langle \vec{P}(t_a) \rangle = 0.1$ (Red line) The initial conditions are chosen so that 10% of sites are assigned the value $P_i(t = 0) = \xi_i$, where ξ_i is taken from a uniform distribution in the range $[0,0.5]$. For reference we have overlaid the steady state $\langle P \rangle$ of the deterministic mean field theory. Dashed line indicates the excitability $r = r_c$.

Chapter 6: Conclusion

We developed a simplified stochastic model of Ca wave nucleation in a cardiac cell. In this setting, the spatiotemporal dynamics can be characterized using the excitability r , which is the amount of Ca released during a spark, and the spatial coupling s , which is the ratio of the distance Ca ions diffuse during a spark to the average spacing between release sites. In terms of these parameters we show, in Fig.6.1, an illustration of the phase diagram of the system. Here, we identify a critical line (red dashed line) that separates pinned and propagating excitation fronts. This transition line has been observed in previous studies and is due to the spatial discreteness of the system [12,13]. In effect, the spatial separation between release sites ensures that there is always a critical excitability below which waves cannot propagate. A numerical study of the regime of propagation revealed that the waiting time to a nucleation event diverges as the excitability is reduced towards the propagation threshold. Furthermore, we show that as the critical line is approached wave nucleation tends to occur at regions in which the leading eigenvector of the connectivity matrix C_{ij} is peaked. In this regime it is the spatial arrangement of release sites that dictates where fluctuations initiate wave nucleation. However, further away from the critical line there is a regime of high excitability where small fluctuations are sufficient to nucleate waves. In this regime fluctuations dominate nucleation kinetics and the arrangement of CRUs does not play an important role. In particular, in the limit of large r wave nucleation occurs at the first $0 \rightarrow 1$ transition, so that wave nucleation occurs at any site with equal probability. Now, below the critical line we also observe rich dynamical behavior. In particular, we identify a multistable phase where the steady state activity levels form random patterns that are dictated by the initial conditions. In this regime waves do not

propagate and so there is no mechanism to drive the system to the fully active state. Reducing the excitability further we also identify a phase where the system is trapped in a low activity state. In this regime cooperativity between release sites is weak and the system can be described as a collection of independent sites.

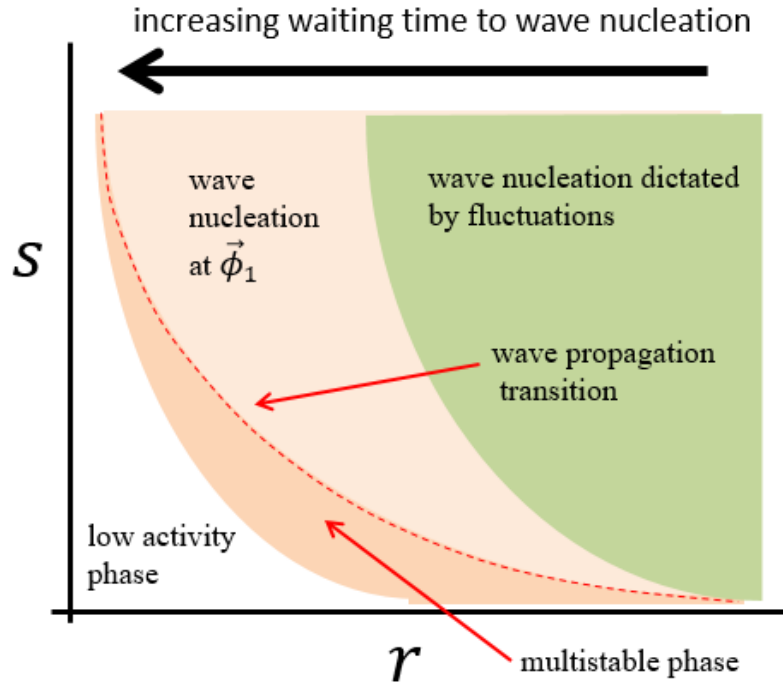


Figure 6.1 Illustration of the system phase diagram.

The rich spatiotemporal dynamics of our system can be explained by the interplay between noise and the time evolution of the deterministic mean field equations (Eq. 5). For large excitability ($r > r_c$) the deterministic mean field equations possess propagating wave solutions, and the quiescent state is unstable since $\lambda_1 > 0$. In this regime wave nucleation is deterministic and the presence of advancing fronts ensures that the same steady state is reached independently of initial conditions. In effect, propagating fronts smooth out homogeneities and the presence of noise does not change the qualitative behavior of the

system dynamics. Now, for $r_b < r < r_c$ the deterministic mean field equations exhibits bistability since the quiescent state with $P_i \sim 0$ is stable ($\lambda_1 < 0$). In this regime fronts advance in the system so that the active branch with $\langle P \rangle \sim 1$ can be reached only if there is a sufficiently large region of active sites. Now, in the presence of noise, fluctuations can induce a large enough region of active sites that will propagate in the system. Thus, the time evolution of the quiescent state will be governed by stochastic wave nucleation, which is characterized by a mean-first-passage time T . In effect, bistability will only be observed in the fully stochastic system if the state of the system is evaluated at a time $t < T$. For $t > T$ wave nucleation will likely occur and bistability will not be observed, as the system will evolve towards the active branch. Now, in the regime $r_a < r < r_b$ the deterministic mean field equations evolve towards a multitude of possible steady states. In this phase we find that active fronts are pinned, so that different steady states can be reached depending on the initial configuration of active sites. Now, in the presence of noise we find that the system evolves towards a smaller set of steady states. This is because noise fluctuations can destabilize a subset of the steady states that are reached by the deterministic evolution. A pertinent analogy to this behavior is found in the theory of spin glasses where a disordered system possesses a rugged energy landscape with a large number of energy minima[21]. There, fluctuations due to temperature can induce transitions between local minima, and the long time dynamics of the system is governed by the slow dynamics of stochastic escape between these local minima. However, this dynamics is exceedingly slow since the mean time to escape can be exponentially long. In this case the system is said to exhibit "glassy" behavior since the system ages over a long time scale, and steady state may not be reached in a tractable simulation time. In effect,

the presence of noise should drive the system to a unique steady state, but this will likely take an exceedingly long time. Finally, for $r < r_a$ a wide range of initial conditions evolve to the same quiescent state with $P_i \sim 0$. In this regime there is effectively only one distinct steady state and noise does not change the system behavior.

Our mean field analysis provides a precise picture of the sites of wave nucleation. In the case when $\lambda_1 > 0$ wave nucleation is deterministic and the sites of nucleation tend to occur at the regions where $\vec{\phi}_1$ is localized. However, in the case where the quiescent state is stable ($\lambda_1 < 0$) we find that the leading eigenvector is still predictive of the sites of nucleation. In fact, our numerical analysis showed that as r is decreased towards the propagation threshold, the correlation between the leading eigenvector and the sites of wave nucleation increases. This result can be explained from the fact that small fluctuations around the quiescent state evolve according to Eq. 10. Thus, fluctuations which occur at regions where $\vec{\phi}_1$ is localized will decay exponentially at the rate λ_1 , which is the slowest decay rate in the system. Therefore, we expect that fluctuations in this region will have the highest likelihood to initiate a propagating wave. These results indicate that the spectra of the connectivity matrix plays a crucial role in the escape rate dynamics of the system.

One basic limitation of this study is that we have modeled a Ca spark as a simple stochastic on-off process. However, in a cardiac cell excitation of a Ca spark depends on recovery processes which originate either from recovery from inactivation of the RyR channel, or the replenishing of the SR load following Ca release. In effect the excitability of a CRU is itself a time dependent process which will play a crucial role in the location and timing of Ca waves. Hence, our analysis only applies to the dynamics of wave nucleation after

steady state has been reached, and does not apply when recovery processes play a role. Nevertheless, we stress that our simplified analysis is essential to more fully understand the role of spatial geometry, which may not be evident in a more complicated setting.

A second limitation of our study is that we have not explored the role of site-to-site heterogeneities. Recent experimental studies have shown that the distribution of RyR clusters in cardiac myocytes is broadly distributed. This result implies that heterogeneities in a myocyte are substantial and will dictate the formation of SCR. In fact, it is very likely that clusters with a much larger than average number of channels could potentially drive the initiation of SCR. Hence, while our simplified approach neglects these key factors, it allows us to study the interplay between fluctuations and geometry in the nucleation of Ca waves, and further refinement of these ideas will be necessary to make direct contact with experiments.

Bibliography

- [1] M. D. Bootman and M. J. Berridge. The elemental principles of calcium signaling. *Cell Press* 83(1):675-678, 1995
- [2] D. M. Bers. Cardiac excitation-contraction coupling. *Nature* 415(1): 198-206, January 2002
- [3] H. Cheng and W. J. Lederer. Calcium Sparks. *Physiol. Rev.* 88(1): 1491-1545, 2008
- [4] L. T. Izu, W. G. Wier, and C. W. Balk. Evolution of cardiac calcium waves from stochastic calcium sparks. *Biophys. J.* 80(1): 103-120, January 2001.
- [5] T. Takamatsu and W. G. Wier. Calcium in mammalian heart: quantification of origin, magnitude, waveform and velocity. *FASEB J.*: 4-1519 , 1990.
- [6] W. Chen, G. Aistrup, J. A. Wasserstrom, and Y. Shiferaw. A mathematical model of spontaneous calcium release in cardiac myocytes. *Am. J. Physiol: Heart Circulatory Physiol.* 300(1): H1794-H1805, 2011.
- [7] E. G. Lakatta, M. C. Capogrossi, A. A. Kort, and M. D. Stern. Ryanodine releases calcium from sarcoplasmic reticulum in calcium-tolerant rat cardiac myocytes. *Fed. Proc:* 44-2977, 1985.
- [8] R. P. Katta and K. R. Laurita. Cellular mechanism of calcium-mediated triggered activity in the heart. *Circulation Res.* 96(1): 535-542, 2005.
- [9] W. Chen, M. Asfaw, and Y. Shiferaw. The Statistics of calcium-mediated focal excitations on a one-dimensional cable. *Biophys. J.* 102(1), 461-471, February 2012.
- [10] R. F. Gilmour, Jr. and N. S. Moise. Triggered activity as a mechanism for inherited ventricular arrhythmias in German shepherd dogs. *J. Am. Coll. Cardiol.* 27(1): 1526-1533, 1996.
- [11] K. R. Laurita and R. P. Katta. Delayed afterdepolarization-mediated triggered activity associated with slow calcium sequestration near endocardium *J. Cardiovasc. Electrophysiol.* 16(1): 418-424, October 2005.
- [12] M. Bar, M. Falcke, H. Levine, and L. S. Tsimring. Discrete stochastic modeling of calcium channel dynamics. *Phys. Rev. Lett.* 84(1): 5664-5667, June 2000.
- [13] M. Falcke, L. Tsimring, and H. Levine. Stochastic spreading of intracellular Ca release. *Phys. Rev. E* 62(1): 2636-2643, August 2000.
- [14] M. Nivala, P. Korge, M. Nivala, J. N. Weiss, and Z. Qu. Linking flickering to waves and whole-cell oscillations in a mitochondrial network model. *Biophys. J.* 101(1): 2102-2111, November 2011.
- [15] M. Nivala, C. Y. Ko, M. Nivala, J. N. Weiss, and Z. Qu. The emergence of subcellular pacemaker sites for calcium waves and oscillations. *J. Physiol:* 591-5305, 2013.
- [16] M. Nivala, C. Y. Ko, M. Nivala, J. N. Weiss, and Z. Qu. Criticality in intracellular calcium signaling in cardiac myocytes. *Biophys. J.* 102-2433, 2012.

- [17] J. S. Marchant and I. Parker. Role of elementary Ca puffs in generating repetitive Ca oscillations. *EMBO J.* 20(1): 65-76, 2001.
- [18] C. Franzini-Armstrong, F. Protasi, and V. Ramesh. Shape, size, and distribution of Ca release units and couplons in skeletal and cardiac muscles. *Biophys. J.* 77(1): 1528-1539, September 1999.
- [19] C. Franzini-Armstrong, F. Protasi, and P. Tijsskens. The assembly of calcium release units in cardiac muscle. *Ann. N. Y. Acad. Sci.* 1047(1): 76-85, 2005.
- [20] M. Fill and J. A. Copello. Ryanodine receptor calcium release channels. *Physiol. Rev.* 82(4): 893-922, 2002.
- [21] M. Naraghi and E. Neher. Linearized Buffered Ca^{2+} Diffusion in Microdomains and Its Implications for Calculation of $[\text{Ca}^{2+}]$ at the Mouth of a Calcium Channel. *J. Neurosci.* 17(18): 6961-6973, September 1997.
- [22] M. Falcke and D. Malchow. Understanding calcium dynamics: Experiments and theory, lecture notes in physics. Springer, Berlin, 2003.
- [23] J. A. Hertz and K. H. Fischer. Spin Glasses. Cambridge University Press, Cambridge, 1991.
- [24] P. B. Simpson, S. Mehotra, G. D. Lange, and J. T. Russell. High density distribution of endoplasmic reticulum proteins and mitochondria at specialized Ca release sites in oligodendrocyte processes. *J. Biol. Chem.* 272(1): 22654-22661, 1997.
- [25] D. Baddeley, I. D. Jayasinghe, L. Lam, S. Rossberger, M. B. Cannell, and C. Soeller. Optical single-channel resolution imaging of the ryanodine receptor distribution in rat cardiac myocytes. *Proc. Natl. Acad. Sci. USA* 106(1):22275-22280 (2009).
- [26] Arnold M. Katz. Physiology of the heart. Lippincott Williams & Wilkins, 2001.
- [27] Hou Y, Jayasinghe I, Crossman DJ, Baddeley D, Soeller C. Nanoscale analysis of ryanodine receptor clusters in dyadic couplings of rat cardiac myocytes. *J Mol Cell Cardiol* ;80:45–55, 2015.
- [28] Shiferaw, Y, Aistrup, G. L. and Wasserstrom, J. A. Intracellular Ca^{2+} waves, afterdepolarizations, and triggered arrhythmias. *Cardiovasc. Res.* 95:265–268, 2012.
- [29] Chen X, Guo L, Kang J, Hou Y, Wang S, and Tan W. Calcium waves initiating from the anomalous subdiffusive calcium sparks. *Journal of the royal society, Interface/the Royal Society* 11: 20130934, 2014.
- [30] Karma A. Physics of Cardiac arrhythmogenesis. *Annu. Rev. Condens. Matter Phys.* 4: 313-337, 2013.
- [31] Stokke M.K., Rivalsrud F., Sjaastad I., Sejersted O.M., Swift F. From global to local: a new understanding of cardiac electromechanical coupling. *Tidsskr. Nor.Laegeforen.*, 12-13: 1457-1460, 2012.

